communications chemistry

A Nature Portfolio journal

Article

https://doi.org/10.1038/s42004-025-01855-x

Synergistic 3D π–π networks enforce persistent foldamer configuration with tunable full-color circularly polarized luminescence

Hao Hu[1,5], Qiangsheng Zhang[1,5], Ziyan Wu[1], Hongtao Liu[1], Jialin Xie[1], Zhenchang Wen[2], Weijie Chi[1], Jianwei Li[3,4] ✉ & Chunman Jia[1,2] ✉

Achieving molecular chirality with enantiostability in purely π-conjugated foldamers remains a substantial challenge due to inherently weak π-π stacking interactions and facile racemization. Herein, we introduce a novel design strategy employing synergistic intramolecular 3D π–π stacking networks within a 1,8-diarylnaphthalene framework, enabling foldamers to exhibit extraordinary configurational stability. A systematic series of quinoxaline- and phenazine-based foldamers incorporating carbazole (CZ) and diphenylamine (DPA) donors were synthesized, with chiral configurations stabilized through complementary face-to-face and laterally offset π–π stacking interactions. Single-crystal X-ray analyses and computational studies confirmed the formation of complex intramolecular π-networks, providing exceptional racemization barriers ($\Delta G^{\ddagger}$ up to 26.06 kcal mol^{-1}), exceeding conventional atropisomers. Additionally, the modular donor-acceptor design facilitates full-color circularly polarized luminescence (469–684 nm), maintaining high dissymmetry factors ($|g_{lum}| > 10^{-3}$) across solution and solid-state environments. This work establishes a generalizable principle for constructing chiral foldamers with enantiostability and tunable optical properties through tailored 3D aromatic interactions, offering significant advances in chiral optoelectronics and responsive materials.

Foldamers are synthetic oligomers designed to adopt predictable and stable three-dimensional conformations[1–8]. They have emerged as a central research area in supramolecular chemistry and materials science, with profound implications spanning from molecular recognition and catalysis to advanced optoelectronic and photonic applications[9–13]. Aromatic foldamers, in particular, have attracted substantial attention owing to their intrinsic ability to form stable secondary structures through π–π stacking interactions[14–18]. Unlike hydrogen bonding or metal coordination, π–π stacking provides an intrinsically reversible, dynamic, yet relatively weak stabilizing force, posing significant challenges in achieving molecular chirality with enantiostability[14–18]. Thus, while aromatic stacking interactions can drive the initial formation of chiral folds, maintaining long-term structural integrity and enantiopurity under ambient conditions remains a formidable scientific and synthetic challenge.

To date, a variety of strategies have been explored to enhance the configurational stability of chiral aromatic foldamers. Notably, approaches such as bulky substituent incorporation, macrocyclization, and the introduction of additional covalent interactions have been employed to elevate the energetic barrier of racemization[19–25]. For example, previous reports on ortho-phenylene oligomers demonstrated controlled helical folding mediated by offset face-to-face aromatic interactions[26–29]. However, these systems typically suffer from rapid conformational interconversion, limiting their practical applications in chiral optoelectronic technologies. Similarly, chiral aromatic oligoamide foldamers incorporating pyrene excimers or macrocyclic aggregates demonstrated stable chiroptical properties but generally lacked broad tunability in their emission colors[30–34]. Achieving foldamers with both exceptionally high racemization barriers and modularly tunable chiroptical properties like full-color circularly polarized luminescence

[1]Hainan Provincial Key Lab of Fine Chem, School of Chemistry and Chemical Engineering, Hainan University, Haikou, China. [2]Analytical & Testing Center (Center for Advanced Studies in Precision Instruments), Hainan University, Haikou, China. [3]MediCity Research Laboratory, University of Turku, Turku, Finland. [4]Macao Institute of Materials Science and Engineering, Macau University of Science and Technology, Taipa, Macau, SAR, China. [5]These authors contributed equally: Hao Hu, Qiangsheng Zhang. ✉e-mail: lijianwei@must.edu.mo; jiachunman@hainanu.edu.cn

(CPL) remains relatively unexplored and represents an urgent frontier in advanced functional materials.

Li et al. recently developed a novel class of multilayer 3D chiral architectures that show particular promise for resolving the aforementioned issues[7,8,35–46]. Building upon this, we envisioned an innovative approach based on the strategic construction of intramolecular 3D π–π stacking networks within a modular, π-conjugated aromatic foldamer scaffold. Specifically, we report herein a series of novel 1,8-diarylnaphthalene-derived foldamers featuring quinoxaline (Qx) and phenazine (Pz) acceptor units coupled with carbazole (CZ) or diphenylamine (DPA) donors, carefully designed to leverage the cooperative interplay of diverse π–π stacking motifs (Fig. 1). Unlike traditional foldamers that typically rely on a single dominant stacking interaction or planar stacking interface[46–48], our design systematically integrates multiple complementary stacking geometries, including co-facial, offset, and T-shaped interactions[49,50]. This synergistic combination establishes a robust 3D aromatic network, dramatically enhancing configurational stability and raising the racemization energy barriers ($\Delta G^{\ddagger}$ up to 26.06 kcal mol^{-1}) beyond conventional atropisomerization thresholds. Crucially, single-crystal X-ray crystallography clearly demonstrates that our foldamers adopt stable, inherently chiral configurations stabilized by a complex intramolecular 3D network of π–π interactions involving both electron-rich and electron-poor aromatic components. Comprehensive structural and computational analyses, including interaction region indicator (IRI) and energy decomposition analyses (EDA), reveal the origin of this configurational persistence as arising from a delicate balance between directional van der Waals interactions, steric effects from strategically placed tert-butyl substituents, and optimal overlap of complementary electron-donor and acceptor π-surfaces. Remarkably, these analyses uncover how subtle changes in stacking geometry or substituents can profoundly influence enantiostability, thereby providing fundamental insight into the rational molecular design of configurationally stable foldamers. Beyond achieving exceptional stereochemical control, our design platform simultaneously enables precise tuning of the foldamers' optoelectronic properties. By modulating donor-acceptor pairs and substituent electronic effects, we successfully achieved modular full-color photoluminescence spanning from blue to deep red (469–684 nm), with pronounced intramolecular charge-transfer (ICT) transitions clearly verified by extensive spectroscopic and theoretical studies. Significantly, chiral foldamers exhibited robust CPL both in solution and solid states, characterized by high dissymmetry factors ($|g_{lum}| > 10^{-3}$), thereby positioning our foldamer series as promising candidates for emerging chiral photonic applications such as circularly polarized OLED displays, chiral sensing, bio-imaging, and optically active security inks[51–54]. Therefore, this work advances the foldamer concept by presenting a fundamentally novel strategy—exploiting synergistic intramolecular 3D π–π stacking networks—to achieve molecular chirality with enantiostability and versatile optical functionality in fully organic π-systems. Through careful design, we deliver simultaneously enhanced configurational stability, sophisticated structural complexity, and finely adjustable optoelectronic performance within a single chiral architecture. This integrated design principle not only provides a profound advancement in foldamer chemistry but also lays critical groundwork for future generations of chiral functional materials, where stability, versatility, and tunability are of paramount importance.

Results and Discussion

Design and synthesis of 3D π-network foldamers

Consistent with our molecular design strategy outlined in the introduction, to investigate the synergistic effects of intramolecular π-π interaction, we designed and synthesized two novel foldamer series featuring C_2-symmetric architectures, quinoxaline-based (Qx) and phenazine-based (Pz). In this molecular framework, the quinoxaline (Qx) and phenazine (Pz) moieties served as electron-accepting units, while carbazole (CZ) and diphenylamine (DPA) derivatives were incorporated as the elongated electron-donating units, which were widely used as the advanced D-A type luminescent emitters[55–57]. Naphthalene served as π-conjugated linkers between donor and acceptor moieties. These racemic compounds were synthesized via Pd-catalyzed Suzuki-Miyaura cross-coupling under the optimized conditions, achieving isolated yields of 87-94% (Fig. 2a and synthetic details in Supplementary Information-section 2). Systematic substitution generated six derivatives: **Qx-CZ, Qx-CZ-tBu, Qx-DPA-tBu, Pz-CZ, Pz-CZ-tBu** and **Pz-DPA-tBu** (Fig. 2b, c), where t-Bu groups increase steric hindrance and further enhance the electron-donating effect (full characterization by NMR, HR-MS data in Supplementary Information-section 3). Chiral HPLC resolution using a Daicel CHIRALPAK IF column (n-hexane/CH_2Cl_2) successfully separated all racemic mixtures into enantiopure forms (The highest e.e. up to 99%, verified by analytical HPLC in Fig. S35-S40; proportion of mobile phase and retention times in Tables S1, S2). Thermal

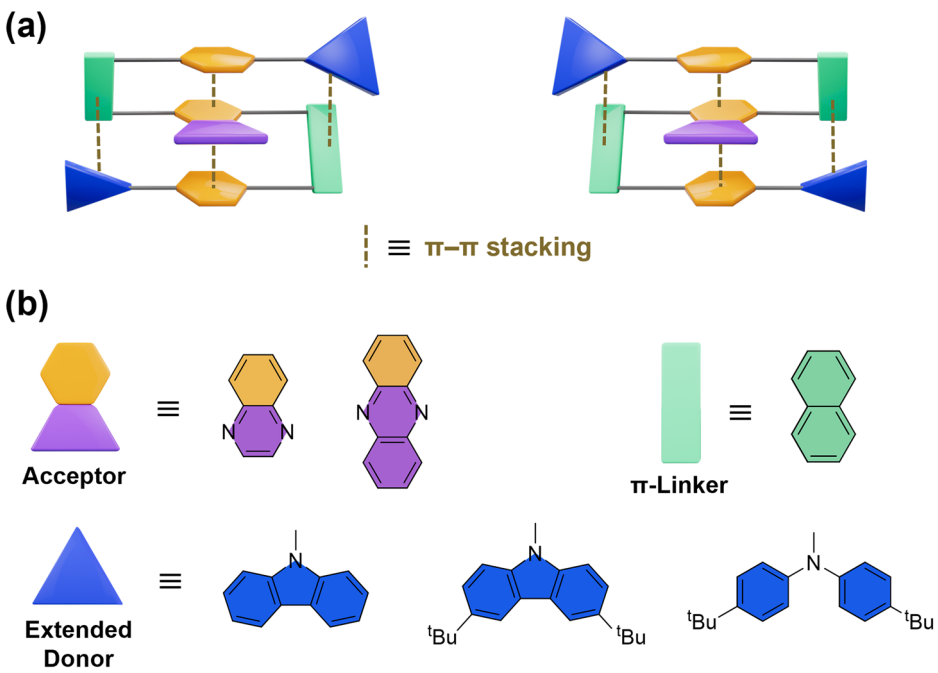

Fig. 1 | Conceptual model. a conceptual model of the synergistic 3D π–π network that stabilizes the chiral foldamer configuration, **b** building blocks constituting the 3D π–π network.

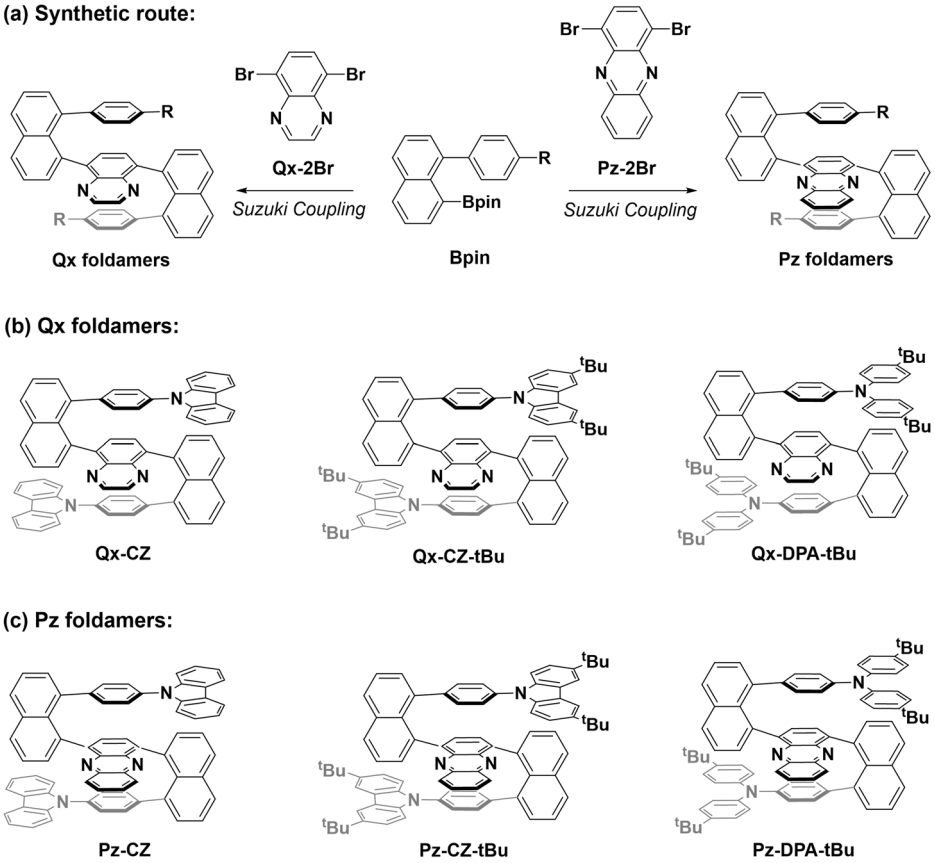

Fig. 2 | Synthesis and structures. a key synthetic steps, structural formulas of **b Qx foldamers** and **c Pz foldamers**.

analysis revealed exceptional stability across the series, with 5% weight-loss temperatures (T_d) ranging from 469 °C to 496 °C (Fig. S78-S83).

Single-crystal structure of chiral foldamers

To verify structural assumptions from the synthesis and ensure molecular chirality, single crystals of enantiopure **Qx-CZ-tBu** were grown by slow diffusion from a solution in CH_2Cl_2 to methanol. X-ray crystallographic analysis (CCDC: 2393433 and 2393434) unambiguously confirmed the mirror-image relationship (Fig. 3a, b and Supplementary Data 1 and 2) between the two enantiomers, as evidenced by their flack parameters of 0.204 and 0.037 (Tables S3 and S4). Both enantiomers of **Qx-CZ-tBu** adopt a chiral folded configuration devoid of symmetry planes or inversion centers (Fig. 3a, b). Taking the single crystal of **Qx-CZ-tBu** (Fig. 3b) as an example, the central quinoxaline (R_4) engages in nearly coplanar stacking with two benzene rings (R_2 and R_6), exhibiting interplanar distances of 3.5 Å (R_2-R_4, dihedral angle 27.9 °) and 3.6 Å (R_4-R_6, dihedral angle 24.5 °). This face-to-face alignment of the R_2-R_4-R_6 triad establishes a through-space conjugation network mediated by π-π stacking interactions. Notably, offset π-π stacking interactions were observed between naphthalene moieties (R_1 and R_7) and carbazole units (R_3 and R_5), with interlayer distances/dihedral angles of 4.5 Å/7.5 ° (R_3-R_7) and 4.2 Å/19.8 ° (R_1-R_5). Crystallographic packing analysis revealed the absence of intermolecular π-stacked arrays (Fig. 3c). Under analogous crystallization conditions, racemic compounds **Qx-CZ, Qx-CZ-tBu, Qx-DPA-tBu** and **Pz-CZ** (Supplementary Data 3-6) were obtained and found to exhibit similar intramolecular π-stacking motifs. Alternatively, in the single crystal of **Qx-DPA-tBu** (Figure. S45 and Supplementary Data 5), the laterally offset π-π stacking interactions between naphthalene moieties and diphenylamine units were remarkably weakened, with interlayer distances/dihedral angles of 5.7 Å/61.8 ° and 4.6 Å/50.1 °. From the perspective of stacking categories and geometries, these various short-range π-π stacking oriented in different directions synergistically form the intramolecular 3D π-networks of the entire foldamers.

To systematically investigate the π-stacking modulation of non-covalent interactions, we performed Interaction Region Indicator (IRI) analyses to quantify key parameters, including hydrogen bonding, van der Waals (vdW) forces, and steric effects[58]. As shown in Fig. 3d, all six compounds exhibited prominent vdW interactions within their central three-layer and edge dual-layer regions. Notably, systems with planar carbazole (CZ) moieties (**Pz-CZ, Qx-CZ, Pz-CZ-tBu**, and **Qx-CZ-tBu**) demonstrated more remarkable vdW interactions between CZ units and naphthalene groups in laterally dual-layer regions. In contrast, the nonplanar diphenylamine (DPA)-containing analogs (**Pz-DPA-tBu** and **Qx-DPA-tBu**) showed attenuated vdW interactions in edge dual-layer regions accompanied by enhanced steric repulsions. The chiral configurational stability of intramolecular 3D π-networks may be influenced by the energetic compensation between vdW and steric forces.

With these results in hand, we proceeded to determine the absolute configuration of chiral foldamers. As shown in Fig. 3b, it reveals that the structure possesses two chiral axes independently located at R_1-R_4 and R_7-R_4, enabling the formation of (R_a, R_a) or (*M, M*) configurations based on the Cahn-Ingold-Prelog (CIP) rules[59,60], which is analogous to previously reported multi-axially chiral naphthalene oligomers[61]. Simultaneously, this structure exhibits planar chirality[62], reminiscent of classical ansa-type architectures[63,64]. However, unlike the ansa chains that completely rely on covalent bridging motifs, the planar chirality here arises from a hybrid strategy combining dual-layer π-π stacking interactions (R_1/R_5 and R_3/R_7) and covalent cross-linkings (R_1-R_4-R_7-R_6-R_5 and R_7-R_4-R_1-R_2-R_3). As a result, it generates two unsealed yet conformationally strained macrocyclic chains, which may suppress racemization by restricting free rotation of the prochiral face (R_4), thereby enabling the formation of (S_p, S_p) or (*M, M*) configurations. Hence, the enantiomers of these foldamers harbor two chiral fragments, which overlap both axial and planar chirality. Their meso-isomer (*P, M*) is unstable and was not detected in HPLC and NMR due to significant steric hindrance between the top and bottom layers.

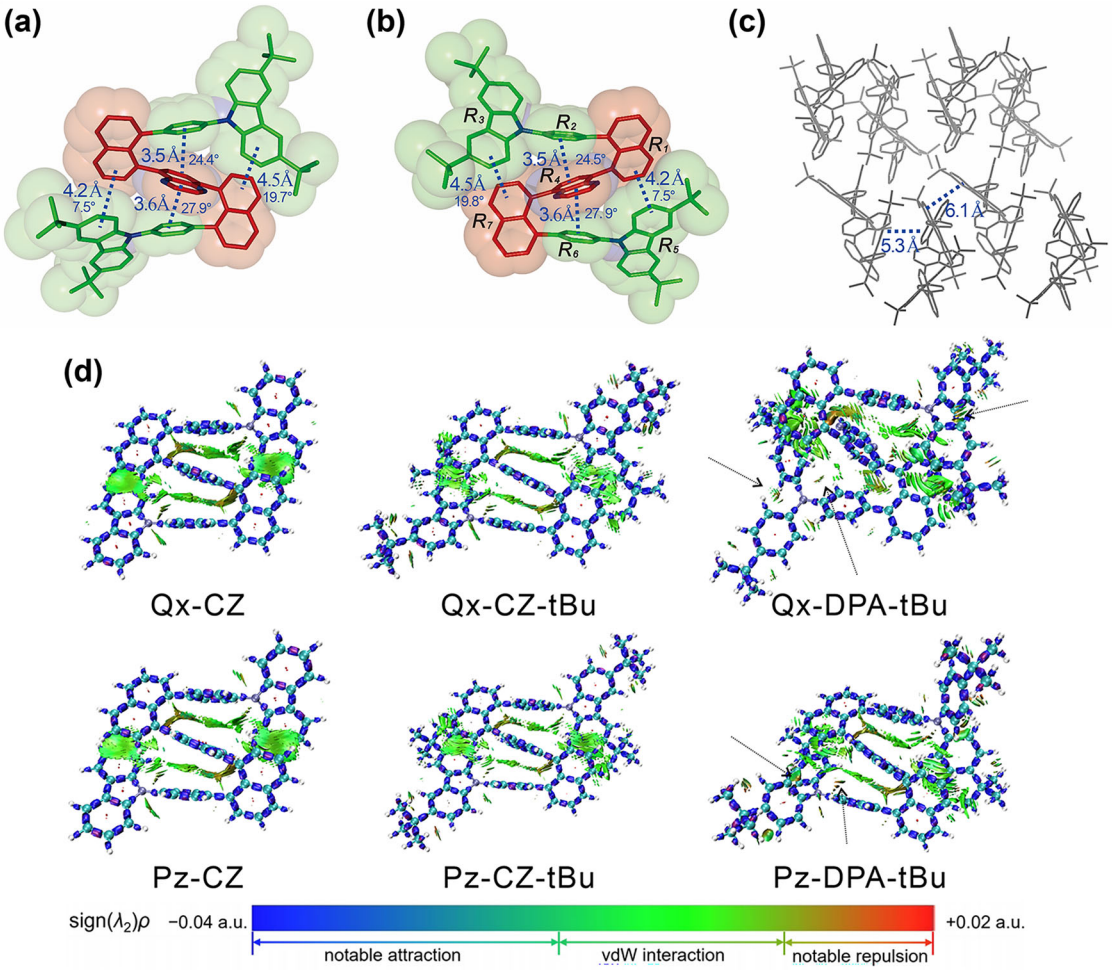

Fig. 3 | Single-crystal structures and intramolecular non-covalent interactions. Single crystal structures of the enantiomers of **Qx-CZ-tBu, a** peak 1 in HPLC, **b** peak 2 in HPLC, and **c** packing of **Qx-CZ-tBu** (peak 2 in HPLC). **d** IRI maps of **Qx-CZ, Qx-CZ-tBu, Qx-DPA-tBu, Pz-CZ, Pz-CZ-tBu**, and **Pz-DPA-tBu**, sign(λ_2)ρ is mapped on IRI isosurfaces according to the color bar.

Table 1 | Summary of k, $t_{1/2}$ and $\Delta G^{\ddagger}$ of enantioenriched Qx-CZ, Qx-CZ-tBu, Qx-DPA-tBu, Pz-CZ, Pz-CZ-tBu and Pz-DPA-tBu

	Qx-CZ	Qx-CZ-tBu	Qx-DPA-tBu	Pz-CZ	Pz-CZ-tBu	Pz-DPA-tBu
k^a (s^{-1})	2.38×10^{-5}	2.23×10^{-7}	4.33×10^{-5}	2.34×10^{-5}	3.62×10^{-7}	4.84×10^{-5}
$\Delta G^{\ddagger}$ (kcal mol^{-1})	23.34	26.06	22.99	23.35	25.78	22.93
$t_{1/2}{}^a$	242.5 min	18 day	133.3 min	247.2 min	11 day	119.3 min

[a]Recorded in CH_2Cl_2 (c = 0.1 mg mL^{-1}) at 293.15 K.

Enantiostability mechanism of chiral foldamers

Building upon structural insights from X-ray crystallography, to elucidate clearly the relationship between the synergistic differences of these π-network foldamers and their enantiostability, we conducted the quantitative assessment through dynamic HPLC analyses monitoring enantiomeric excess (e.e.) decay in CH_2Cl_2 at 293 K (Figs. S47–S52, Tables S9–S14). The resulting data, including rate constants (k), half-lifetimes ($t_{1/2}$), and racemization energy barriers ($\Delta G^{\ddagger}$), are summarized in Table 1. All chiral foldamers exhibited exceptionally available racemization barriers ($\Delta G^{\ddagger}$ = 22.93–26.06 kcal mol^{-1}), surpassing the typical atropisomerization threshold ($\Delta G^{\ddagger}$ = 22.2 kcal mol^{-1}) and confirming room-temperature stereochemical integrity[65]. Furthermore, the variation in foldamer enantiostability originates from the distinct stacking and steric effects between the extended donor groups and the naphthalene rings, whereas the extension of the central electron-acceptor group does not alter the enantiostability. Consequently, their stability falls into three distinct gradients. The lowest $\Delta G^{\ddagger}$ values were provided by the DPA-tBu-modified **Qx-DPA-tBu** and **Pz-DPA-tBu**, at 22.99 and 22.93 kcal mol^{-1}, respectively. The stability of the CZ-modified foldamers was enhanced, with $\Delta G^{\ddagger}$ values of 23.34 and 23.35 kcal mol^{-1} for **Qx-CZ** and **Pz-CZ**. Notably, introducing tert-butyl groups to CZ significantly boosted stability, the $\Delta G^{\ddagger}$ values for **Qx-CZ-tBu** and **Pz-CZ-tBu** increased to 26.06 and 25.78 kcal mol^{-1}, respectively, and the corresponding $t_{1/2}$ at room temperature extended from the order of hours to days (Table 1).

Next, we employed theoretical calculations using Hirshfeld-partitioned Independent Gradient Model (IGMH) analyses coupled with electrostatic potential (ESP) mapping and energy decomposition analysis (EDA)[66–69] to deconvolute the contributions to configurational locking. IGMH analyses revealed that dominant intramolecular interactions, including π-π interactions, C–H···π interactions, and N···H interactions, stabilize the foldamers

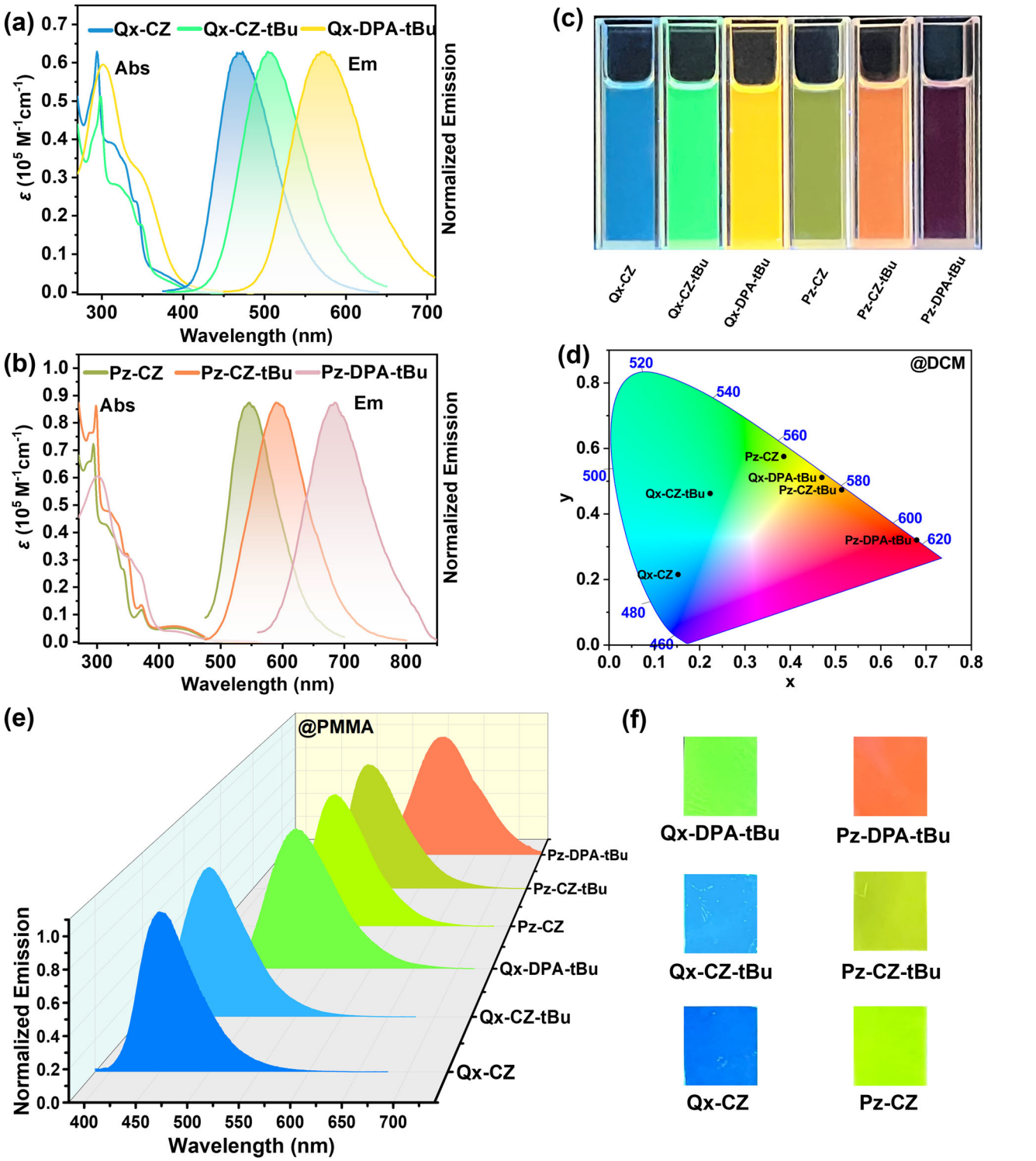

Fig. 4 | Photophysical characterization. Absorption and emission spectra of **a Qx foldamers** and **b Pz foldamers** in CH_2Cl_2 (c = 10 μM), λ_{ex} = 330 nm for **Qx-CZ**, λ_{ex} = 335 nm for **Qx-CZ-tBu**, λ_{ex} = 350 nm for **Qx-DPA-tBu**, λ_{ex} = 345 nm for **Pz-CZ**, λ_{ex} = 350 nm for **Pz-CZ-tBu**, and λ_{ex} = 370 nm for **Pz-DPA-tBu**. **c** Emission photographs under 365 nm UV irradiation and **d** CIE color coordinates of foldamers in CH_2Cl_2 (c = 10 μM). **e** Emission spectra of foldamers in PMMA doped film (w.t.=1%) and **f** emission photographs under 365 nm UV irradiation.

(Figs. S106–S111). It is important to note that, in addition to the π-π interactions formed between the central three layers, the planar CZ groups can form significant additional π-π interactions with the naphthalene rings. In contrast, the π-π interactions between the non-planar DPA-tBu groups and the naphthalene rings are significantly weakened or even absent due to their flexible conformations, leaving primarily C–H···π interactions (Fig. S108). Complementary ESP maps demonstrated charge complementarity between the π-surfaces (negative planar regions vs. positive edges), consistent with directional π-stacking geometries driven by co-facial π-π interactions in the central core and laterally offset π-π stacking (Figs. S99–S104). EDA further quantified steric effects, showing that introducing tert-butyl groups, replacing carbazole with diphenylamine, or

Table 2 | Summary of Optical Properties of Qx-CZ, Qx-CZ-tBu, Qx-DPA-tBu, Pz-CZ, Pz-CZ-tBu and Pz-DPA-tBu

	λ_{abs}[a] (nm)	λ_{em}[a] (nm)	λ_{em}[b] (nm)	Φ[c] (%)	τ_{ave}[d] (ns)	E_{HOMO}[e] (eV)	E_{LOMO}[e] (eV)	ΔE_{DFT}[e] (eV)	E_{HOMO}[f] (eV)	$\Delta E_{optical}$[g] (eV)
Qx-CZ	294,342	469	450	1.1	1.09	-5.425	-2.179	3.25	-5.487	2.94
Qx-CZ-tBu	298,348	506	457	4.9	2.52	-5.267	-2.161	3.11	-5.335	2.96
Qx-DPA-tBu	302,340	572	518	5.8	21.53	-4.922	-2.117	2.81	-4.985	2.88
Pz-CZ	294,342,425	546	525	0.8	1.07	-5.410	-2.693	2.72	-5.488	2.47
Pz-CZ-tBu	298,348,425	595	535	2.1	3.15	-5.231	-2.671	2.56	-5.316	2.47
Pz-DPA-tBu	301,352,425	684	605	2.0	20.69	-4.887	-2.620	2.27	-4.961	2.45

[a] Recorded in CH_2Cl_2 (c = 10 μM) at 298 K. [b] Recorded in PMMA doped films (w.t. = 1%) at 298 K. [c] Emission quantum yields using an integrating sphere, recorded in CH_2Cl_2 (c = 10 μM). [d] Emission lifetime in PMMA doped films. [e] DFT calculations (B3LYP-D3(BJ)/6-311 G(d,p)) for *MM*-enantiomers, $E_{gap(DFT)} = E_{LUMO} - E_{HOMO}$. [f] Measured by cyclic voltammetry (CV) in CH_2Cl_2. [g] E_{gap}(optical): optical energy gap obtained from the absorption spectra onset in CH_2Cl_2.

extending the central core all increase molecular steric hindrance (Fig. S112). For instance, Pauli repulsion energies increased slightly from 1286.19 kcal mol^{-1} (**Pz-CZ**) to 1292.05 kcal mol^{-1} (**Pz-CZ-tBu**) upon tert-butyl substitution. We can infer that further increasing steric effects on the premise of establishing favorable lateral π-π stacking effectively enhances enantiostability. In contrast, steric hindrance alone is insufficient to enhance stability. For example, the increased steric hindrance from extending the central electron-acceptor fails to translate into better enantiostability because the stacking geometry—characterized by an open dihedral angle—remains unchanged and fails to improve the effectiveness of configurational locking. These analyses reveal that the enantiostability of chiral foldamers arises from a synergistic interplay of multiple π-π stacking interactions in a 3D π-network: directional co-facial and offset π-π stacking lock the chiral configuration, whereas only when positioned within a geometry conducive to π-π stacking can sterically hindering tert-butyl groups further restrict changes in the local conformation and enhance the configurational stability of the entire molecule, underscoring the prerequisite role of the stacking geometry.

Photoluminescence properties of chiral foldamers

Given the structural stability confirmed above, we further explored how intramolecular π–π interactions influence luminescence behaviors[70–72], it encouraged us to investigate the photoluminescence properties of foldamers in different solutions and solid conditions. The UV-vis absorption profiles of six chiral foldamers exhibited structure-dependent variations in CH_2Cl_2 (Fig. 4a, b; Table 2). Characteristic π-π transitions dominated the 300–330 nm region, while intramolecular charge-transfer (ICT) transitions appeared at 350-430 nm[73]. Notably, tert-butyl functionalization of carbazole donors induced a 6 nm bathochromic shift in **Qx-CZ-tBu** (348 nm vs. 342 nm for **Qx-CZ**), consistent with enhanced electron-donating capacity. Extended π-conjugation in phenazine-containing systems (e.g., **Pz-CZ** at 425 nm) generated low-energy absorption tails, as corroborated by TD-DFT simulations (Fig. S105) revealing donor-to-acceptor spatial charge transfer.

Photoluminescence spectra demonstrated pronounced polarity-responsive redshifts by ICT effect, with **Qx-CZ-tBu** exhibiting a 68 nm bathochromic shift from hexane (452 nm) to DMF (520 nm) (Fig. S56, Table S15). Systematic donor and acceptor variation enabled full-color emission tuning (blue to red) in CH_2Cl_2 through electronic-donating strength modulation (wavelength: DPA-tBu > CZ-tBu > CZ) and acceptor π-extension (wavelength: Pz > Qx), which is shown in Fig. 4a, d and summarized in Table 2. Taking the **Qx-CZ** as an example, tert-butyl substitution redshifted emission to **Qx-CZ-tBu** by 37 nm (469 → 506 nm), while phenazine incorporation induced a 77 nm shift (469 → 546 nm from **Qx-CZ** to **Pz-CZ**). Frontier orbital analysis revealed the HOMO and LUMO are mainly distributed on the donor and acceptor fragments, respectively, whereas the naphthyl linkers hardly participate in the HOMO and LUMO distribution, leading to a weak overlap between the D and A electronic clouds, and this effect becomes more pronounced with enhanced electron donors (D) and acceptors (A), resulting in barely any HOMO-LUMO overlap in **Pz-DPA-tBu** (Fig. 5). It suggested the possibility of through-space charge-transfer (TSCT) from donor to acceptor.

In addition, the AIEE phenomenon was prominently observed in DMF/H_2O mixtures. For example, **Qx-CZ** exhibits a 14-fold fluorescence enhancement and a 15 nm hypsochromic shift from pure DMF to 50% water content (Fig. S54), underscoring the structural dependence of emission behavior on microenvironmental changes. Dynamic light scattering confirmed nanoparticle formation (d = 99 nm), due to restricted intramolecular rotation in aggregates suppressed nonradiative decay. Based on this result, we performed the solid-state emission of six compounds, tuning persisted in PMMA doped films, maintaining full-color region (Fig. 4e, f). Transient fluorescence analyses revealed donor-dependent lifetime modulation, with DPA systems exhibiting about 20-fold longer lifetimes (21.53 ns for **Qx-DPA-tBu**) versus carbazole analogs (1.09 ns for **Qx-CZ**) (Table S16).

Cyclic voltammetry (CV) measurements also revealed systematic modulation of frontier orbital energies across the foldamer series. Based on the oxidation curve of cyclic voltammetry (Fig. S72–S77, Table 2), the HOMO energy level of the six foldamers were estimated to be −5.487, −5.335, −4.985, −5.488, −5.316 and −4.961 eV with the equation $E_{HOMO} = -[E_{ox} - E_{(Fc/Fc+)} + 4.8]$ eV, which agreed with the theoretically calculated E_{HOMO}. This indicated that the stronger donor (DPA-tBu > CZ-tBu > CZ) resulted in a higher E_{HOMO}. In addition, the level gap (ΔE_{opt}) from the UV/Vis absorption spectrum of the six foldamers was also agreed with calculated ΔE_{DFT} data, and the LUMO energy level were estimated to be −2.547, −2.375, −2.105, −3.018, −2.846 and −2.511 eV with the equation of $E_{LUMO} = E_{HOMO} + \Delta E_{opt}$ which indicated that the extended conjugated acceptor (Pz > Qx) resulted in the lower E_{LUMO}. Based on calculated emission process and optical experiments, it was deduced that ICT emissions of six foldamers arose from $S_1 \rightarrow S_0$ deactivation (Tables S19–S30).

Chiroptical properties of foldamers

Having thoroughly characterized the structural and emission properties, we sought to investigate whether the structure induces chiroptical properties, including those in the solid state. As shown in Fig. 6a, b, the circular dichroism (CD) spectra of six enantiomeric pairs in CH_2Cl_2 exhibited mirror-symmetric Cotton effects across their UV-vis absorption regions (230-430 nm), with absorption dissymmetry factors ($|g_{abs}|$) ($g_{abs} = \Delta\varepsilon/\varepsilon$) ranging from 10^{-3} to 10^{-2} (Figure. S84), whose trends agreed with the calculated $|g_{abs}|^{cal}$ data (Table 3 and Fig. S119). For **(*P,P*)-Qx-CZ-tBu**/**(*M,M*)-Qx-CZ-tBu** (Fig. 6a), two distinct Cotton effect regions were observed: a short-wavelength region (300-330 nm) attributed to exciton coupling within the stacked aromatic layers arising from π-π transitions, and long-wavelength charge-transfer bands (350-430 nm) corresponding to intramolecular donor-to-acceptor interactions. Furthermore, the CD spectra of all enantiomers in PMMA doped films were consistent with the Cotton effects observed in solution (Figs. S85–S90). These CD signatures validate the chiral character originating from exciton coupling between π-stacked parallel layers. Theoretical simulations (TD-DFT/B3LYP-D3(BJ)/6-311 G) successfully reproduced both the spectral line shapes and Cotton effect polarities (Fig. 6c, d), enabling unambiguous assignment of the chiral HPLC elution order (Fig. S35–S40): peak1 corresponds to (*P,P*)-configured enantiomers, while peak2 represents (*M,M*)-configured counterparts.

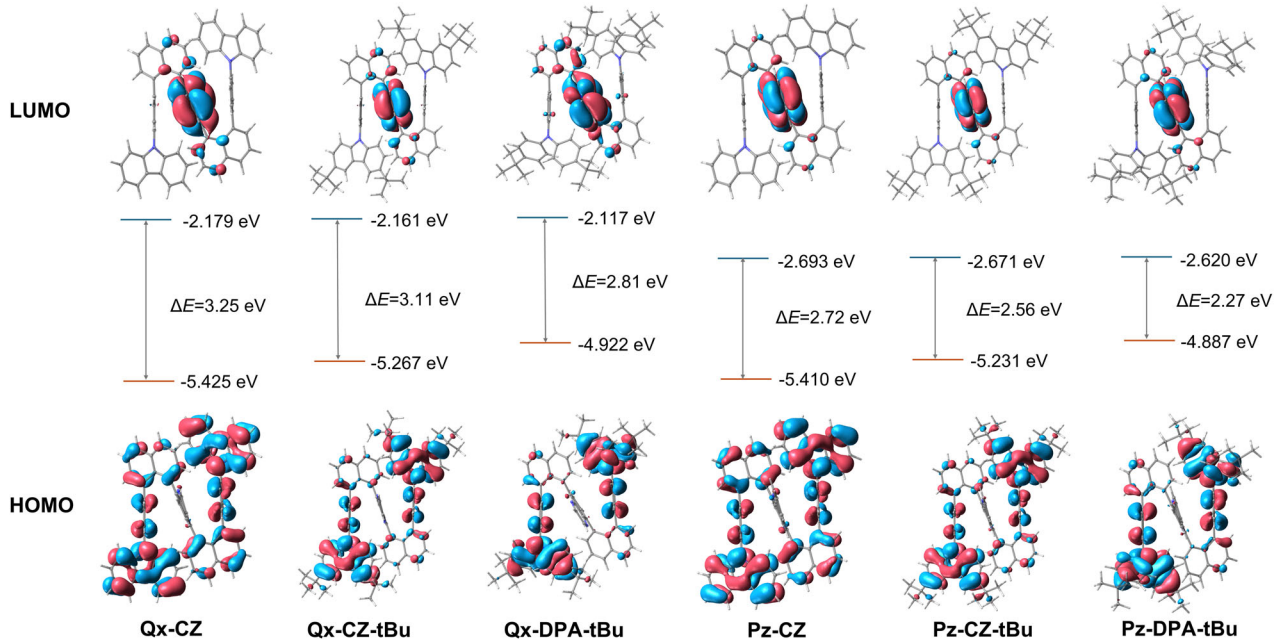

Fig. 5 | Frontier molecular orbital plots. Spatial distributions of HOMOs and LUMOs of **Qx-CZ, Qx-CZ-tBu, Qx-DPA-tBu, Pz-CZ, Pz-CZ-tBu**, and **Pz-DPA-tBu**. Δ*E* is energy gap between HOMO and LUMO.

Fig. 6 | CD spectra. Experimental CD spectra of enantiomers for **a Qx foldamers** and **b Pz foldamers** in CH_2Cl_2 (c = 10 μM). The calculated CD spectra of **c Qx foldamers** and **d Pz foldamers** in CH_2Cl_2.

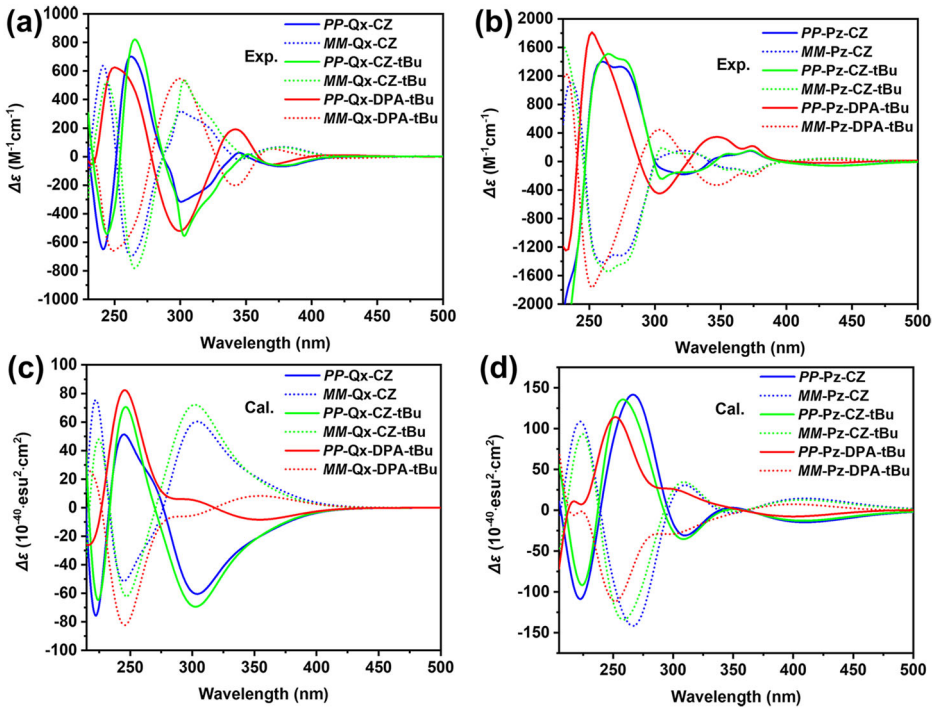

Subsequently, we explored the potential of the foldamers as chiral emitters by measuring their circularly polarized luminescence (CPL) under various conditions. As shown in Fig. 7, the mirror-image CPL spectra of the enantiomers confirmed their chiroptical properties in the excited state. Consistent with the fluorescence emission spectral trends, the CPL spectra of each enantiomer also exhibited wavelength shifts dictated by structural modifications, enabling full-color CPL tunability from blue to red light simply by altering the donor and acceptor units. Under solution conditions, **Qx-CZ** and **Pz-CZ** exhibited notably fluctuating CPL signals with reduced intensities compared to the other four compounds, displaying opposite signs for the same configuration, their luminescence dissymmetry factor ($|g_{lum}|$) were all below 10^{-3} (Figs. 7a, b and S91-S94). In contrast, **Qx-CZ-tBu, Qx-DPA-tBu, Pz-CZ-tBu** and **Pz-DPA-tBu** achieved $|g_{lum}|$ of 2.9×10^{-3}, 2.0×10^{-3}, 3.8×10^{-3} and 4.3×10^{-3}, respectively. Based on the formula: $g_{lum} = 2(I_L - I_R)/(I_L + I_R)$, where I_L and I_R represent the intensities of left and righthanded CPL, precise measurement of I_L and I_R is essential, the low experimental signal-to-noise ratio observed for **Qx-CZ** and **Pz-CZ** in CPL measurements may originate from their weak solution-state emission (low PLQY, see Table S17). Consistent with reports suggesting modulation of the CPL sign by controlling ICT emission[74,75], we anticipate that the stronger donor effects of DPA-tBu and CZ-tBu relative to CZ, modulating the

Table 3 | Summary of Chiroptical Properties of Qx-CZ, Qx-CZ-tBu, Qx-DPA-tBu, Pz-CZ, Pz-CZ-tBu and Pz-DPA-tBu

	CD[a]		$S_0 - S_1$ transition[b]				CPL[a]	$S_1 - S_0$ transition[b]			
	λ [nm]	$\|g_{abs}\|$	$\|\mu\|$ [c]	$\|m\|$ [d]	θ [degree]	$\|g_{abs}\|^{cal}$	$\|g_{lum}\|$	$\|\mu\|$ [c]	$\|m\|$ [d]	θ [degree]	$\|g_{lum}\|^{cal}$
Qx-CZ	302	7.7×10^{-3}	372	1.20	125.3	7.5×10^{-3}	$<10^{-3}$	590	0.78	111.7	2.0×10^{-3}
Qx-CZ-tBu	305	16.8×10^{-3}	146	0.43	42.7	8.6×10^{-3}	2.9×10^{-3}	555	0.71	109.0	1.7×10^{-3}
Qx-DPA-tBu	298	9.2×10^{-3}	175	0.93	83.7	2.3×10^{-3}	2.0×10^{-3}	161	1.07	74.9	7.0×10^{-3}
Pz-CZ	324	4.5×10^{-3}	348	0.60	127.4	4.2×10^{-3}	$<10^{-3}$	507	0.48	123.2	2.1×10^{-3}
Pz-CZ-tBu	306	4.7×10^{-3}	342	0.52	129.3	3.8×10^{-3}	3.8×10^{-3}	503	0.41	126.9	2.0×10^{-3}
Pz-DPA-tBu	304	7.4×10^{-3}	81	0.35	50.4	11.0×10^{-3}	4.3×10^{-3}	75	0.36	65.2	8.1×10^{-3}

[a]Measured in CH_2Cl_2 solutions ($c = 10$ μM). [b]Calculated by TD-DFT at B3LYP-D3(BJ)/6-311 G(d,p) level of theory for *MM*-enantiomers. [c] $|\mu|$ [10^{-20} esu cm]. [d] $|m|$ [10^{-20} erg G^{-1}].

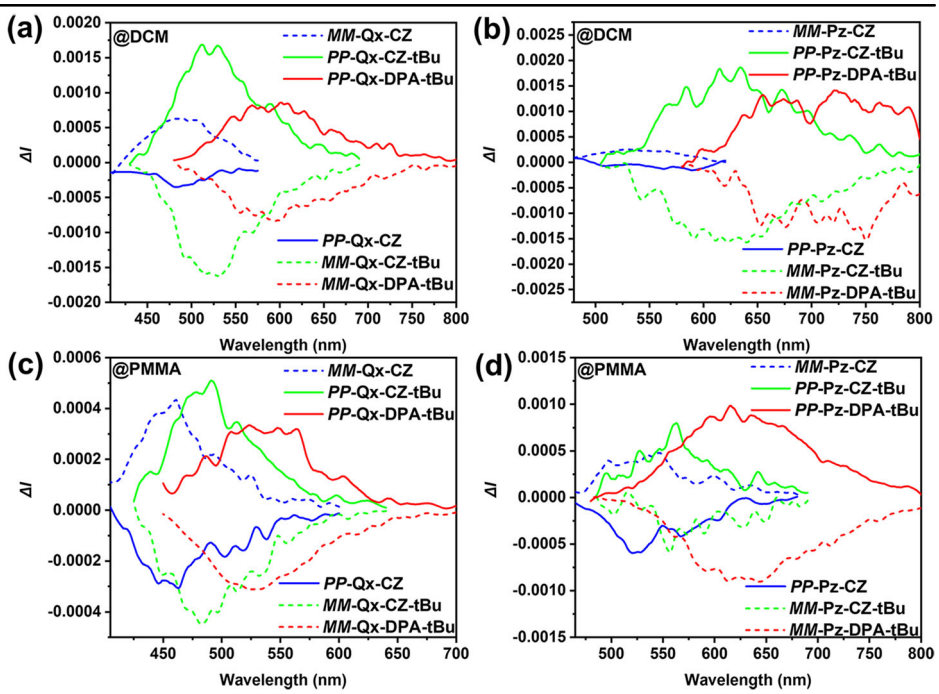

Fig. 7 | CPL spectra. a, **b** CPL spectra of the enantiomers of **Qx foldamers** and **Pz foldamers** in CH_2Cl_2 (c = 10 μM), λ_{ex} = 330 nm for **Qx-CZ**, λ_{ex} = 335 nm for **Qx-CZ-tBu**, λ_{ex} = 350 nm for **Qx-DPA-tBu**, λ_{ex} = 345 nm for **Pz-CZ**, λ_{ex} = 350 nm for **Pz-CZ-tBu** and λ_{ex} = 370 nm for **Pz-DPA-tBu**. **c**, **d** CPL spectra of the enantiomers of **Qx foldamers** and **Pz foldamers** in PMMA doped film.

overall electronic structure of molecules, correlate with their distinct CPL signs. Indeed, when **Qx-CZ** and **Pz-CZ** were dispersed in PMMA doped films (w.t. = 1%) to form solidstate conditions or aggregated in mixed solvents (DMF/H_2O), their CPL signals and g_{lum} curves became relatively smooth and recognizable, exhibiting aggregation induced CPL enhancement (Figs. 7c, d and S95-S98). Other foldamers with stronger ICT (**Qx-CZ-tBu, Qx-DPA-tBu, Pz-CZ-tBu** and **Pz-DPA-tBu**) exhibited notable CPL emission with g_{lum} values similarly on the order of 10^{-3} in dilute solutions, aggregated states or PMMA doped films (Figs. S91–S98). It is noteworthy that, because the enantiomeric purity of some compounds could not be maintained over extended periods, the experimentally determined g_{lum} values for the four compounds other than **Qx-CZ-tBu** and **Pz-CZ-tBu** (which were perfectly optically pure) are likely underestimated relative to the actual values due to enantiomeric decay reducing the enantiomeric excess.

According to theory, the luminescence dissymmetry factor is described as: $g_{lum} = 4 \times |\mu| \times |m| \times cos\theta / (|\mu|^2 + |m|^2)$, where μ and m are the transition electric dipole moment (TEDM) and transition magnetic dipole moment (TMDM) vectors, respectively, and θ is the angle between μ and m. The TEDM of organic molecules is typically several hundred times larger than the TMDM; therefore, the equation simplifies to $g_{lum} = 4 \times cos\theta \times |m| / |\mu|$. This simplified equation indicates that the key to obtaining higher g_{lum} values is the large ratio of $|m|/|\mu|$ and a large $|\cos\theta|$. To explain the variations in the dissymmetry factors, TD-DFT calculations were performed at the B3LYP/6-31 G level to obtain the $|\mu|$, $|m|$ and θ values for the excited states ($S_1 \rightarrow S_0$ transition) of each enantiomeric compound (Fig. 8 and Table 3). As shown in Fig. 8 and Table 3, markedly, the foldamers using diphenylamine as the electron donor exhibit significantly smaller $|\mu|$ values (161×10^{-20} esu cm for **Qx-DPA-tBu** and 75×10^{-20} esu cm for **Pz-DPA-tBu**), whereas those employing carbazole as the electron donor all possess $|\mu|$ values exceeding 500×10^{-20} esu cm. Concurrently, the variations in $|m|$ values across the compounds are relatively minor. Furthermore, while the foldamers with diphenylamine donors display acute θ angles and those with carbazole donors exhibit obtuse θ angles, this difference exerts minimal influence on the $|cos\theta|$ values. Consequently, the larger calculated $|g_{lum}|^{cal}$ values for **Qx-DPA-tBu** (7.0×10^{-3}) and **Pz-DPA-tBu** (8.1×10^{-3}) are primarily attributed to their smaller $|\mu|$ values. In contrast, the carbazolemodified foldamers achieve $|g_{lum}|^{cal}$ values of approximately 2.0×10^{-3}. Overall, based on experimental and theoretical analysis, the $|g_{lum}|$ of the foldamers is influenced by both electronic effects and geometries—stronger ICT and greater π-extension are more favorable for enhanced CPL performance.

Conclusions

This study demonstrates a strategy for constructing chiral foldamers with enantiostability through synergistic intramolecular 3D π-networks, advancing stereochemical control driven by π-π interactions. By integrating

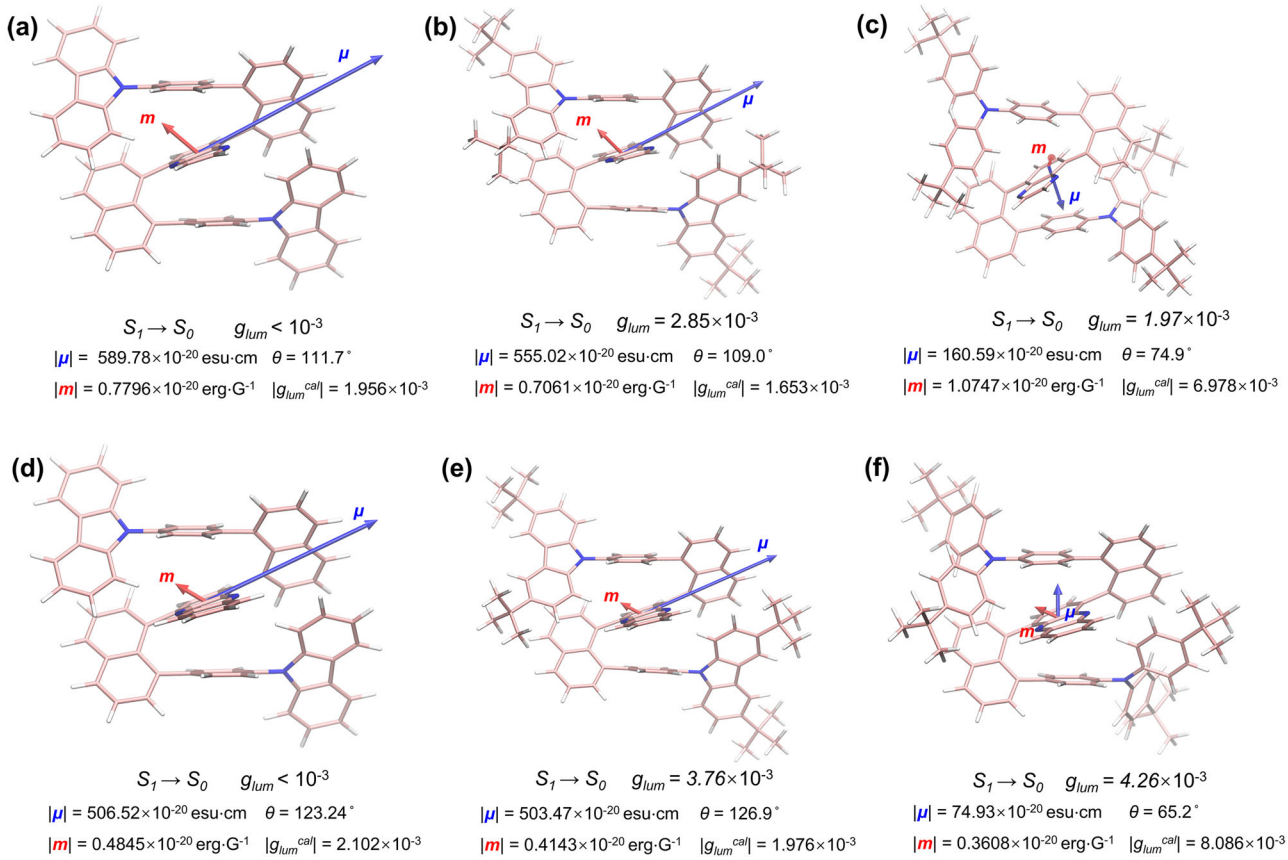

Fig. 8 | Theoretical calculation of the dissymmetry factors. The transition electric dipole vectors (μ) and magnetic dipole vectors (m) in the $S_1 \rightarrow S_0$ transition processes for **a Qx-CZ, b Qx-CZ-tBu, c Qx-DPA-tBu, d Pz-CZ, e Pz-CZ-tBu**, and **f Pz-DPA-tBu**. θ is the angle between μ and m.

central cofacial and laterally offset π-stacking modes within a 1,8-diarylnaphthalene scaffold, we designed foldamers with enhanced configurational stability, achieving racemization barriers ($\Delta G^{\ddagger}$ up to 26.06 kcal mol^{-1}) that exceed conventional atropisomers. Crystallographic and dynamic HPLC analyses reveal that this stability originates from a cooperative triplexπ-stacking network, where face-to-face interactions enforce structural rigidity, while offset donor-acceptor stacking generates torsional asymmetry to lock planar chirality. Peripheral van der Waals interactions and steric enforcement further stabilize the folded architecture. The modular design enables simultaneous control over stereochemical persistence and photoluminescence properties. By tuning donor-acceptor pairs, emission wavelengths are systematically modulated across the broad spectrum (469–684 nm) through intramolecular charge-transfer transitions, while retaining robust circularly polarized luminescence ($|g_{lum}| > 10^{-3}$) in both solution and solid states. This dual functionality, stereochemical stabilization coupled with emissive tunability, resolves the common compromise between structural rigidity and electronic adaptability in chiral materials. Combined experimental and theoretical analyses establish a design framework that correlates π-stacking geometries (co-facial vs. offset) and energy contributions to stereochemical outcomes. These results not only highlight the importance of orchestrated aromatic interactions in stabilizing functional folds but also pave the way for new applications in chiral photonics, sensing, and advanced material science.

Methods

General characterization methods

400 MHz ^{1}H and 100 MHz ^{13}C spectra were recorded on a Bruker spectrometer. High-resolution mass spectral data were obtained on Mass spectra were recorded on a LCMS-IT-TOF or MALDI-TOF MS. Single-crystal X-ray diffraction data were collected on Bruker APEX-I CCD diffractometer. UV-vis spectra were recorded on a SHIMADZU UV-2600. Steady state and transient fluorescence spectra were recorded on HORIBA Fluorolog-3. Fluorescent quantum efficiencies were determined using a Hamamatsu Quantaurus-QY spectrometer (C11347-11). Particle sizes were recorded on Zetasizer nano ZS90.

Electrochemical and thermogravimetric measurements

Cyclic voltammetry (CV) measurements were carried out on a CHI660E (CH Instruments, USA) in a three-electrode cell in an anhydrous CH_2Cl_2 solution of tetrabutylammonium hexafluorophosphate (n-Bu_4NPF_6, 0.1 M) with a scan rate of 100 mV/s at room temperature. All potentials were further calibrated against ferrocene/ferrocenium (Fc/Fc^+). Thermogravimetric analysis was performed with a NETZSCH STA 409 PC/PG thermogravimetric analyzer under nitrogen, heating from 30 °C to 800 °C at a rate of 10 °C/min.

HPLC analysis and racemization kinetics

The separation of isomers with chiral configurations was performed by chiral HPLC and Analytical HPLC was performed on a Waters 2695 instrument equipped with a photodiode array detector and CHIRALPAK columns (4.6 mm × 250 mm, 5 μm) from Daicel Chiral Technologies. Column temperature was maintained at 35 °C. The racemization kinetics experiments were carried out at 20 °C.

Preparation of PMMA films

PMMA (20 mg) and enantiomer (0.2 mg) was dissolved in 1 ml of CH_2Cl_2 in a 2 cm diameter culture dish. The resulting mixture is vaporized at room temperature in a well-ventilated environment to obtain a uniform film that can be used to characterize CD and CPL spectra.

CD and CPL measurements

The CD spectra were measured using a Circular Dichroism spectrometer (Chirascan V100). CPL measurements of solutions and PMMA films were

performed with a circularly polarized luminescence spectrometer (CPL-300, Jasco). The solution is measured as soon as it was configured to prevent the effects of racemization.

Crystal growth

The single crystals of ***Rac*-Qx-CZ, *Rac*-Qx-CZ-tBu**, and ***Rac*-Pz-CZ** were grown by slow diffusion from a solution in CH_2Cl_2 to n-hexane. The single crystals of ***PP*-Qx-CZ-tBu, *MM*-Qx-CZ-tBu**, and ***Rac*-Qx-DPA-tBu** were grown by slow diffusion from a solution in CH_2Cl_2 to methanol.

Theoretical Calculations

All of the simulation calculations were carried out with Gaussian 16 program package[76]. The geometry optimization of all molecules in ground state (S_0) at the level of B3LYP-D3(BJ)/6-311 G(d,p) has been evaluated using the density functional theory (DFT) method. The polarizable continuum model (PCM) was used, with dichloromethane as the solvent. The simulated UV-Vis and ECD spectra were performed by time-dependent density functional theory (TD-DFT) calculations at the CAM-B3LYP-D3(BJ)/6-311 G(d,p) level, and the lowest 100 vertical singlet electronic excited states were formulated. The S_1 geometry of all molecules were optimized at the level of CAM-B3LYP-D3(BJ)/6-311 G(d,p) using the TD-DFT method. The electrostatic potential (ESP) surfaces and independent gradient model based on Hirshfeld partition (IGMH)[66,67] were calculated using the Multiwfn[68] program based on the wavefunction information obtained at the B3LYP-D3(BJ)/6-311 G(d,p) level. The isosurface maps of interaction region indicator (IRI) and Energy Decomposition Analysis (EDA)[69] were calculated at the (B3LYP/6-31 G*) level of theory. The transition electronic and magnetic dipole moments of all enantiomers were calculated by Multiwfn program. All orbitals and isosurfaces were visualized by Visual Molecular Dynamics (VMD) program[77]. The transition electronic/magnetic dipole vectors of all enantiomers were magnified by a factor of 8 to facilitate observation. The transition electronic/magnetic dipole moments ($\boldsymbol{\mu}$, $\boldsymbol{m}$) and dissymmetry factors (g) were calculated based on the literature methods[78,79].

Data availability

All the data and methods are present in the main text, the Supplementary Information and Supplementary Data files. The crystallographic data for structures reported in this article have been deposited at the Cambridge Crystallographic Data Centre (CCDC), under deposition number CCDC 2393434 for ***PP*-Qx-CZ-tBu** [Supplementary Data 1], CCDC 2393433 for ***MM*-Qx-CZ-tBu** [Supplementary Data 2], CCDC 2393430 for ***Rac*-Qx-CZ** [Supplementary Data 3], CCDC 2393432 for ***Rac*-Qx-CZ-tBu** [Supplementary Data 4], CCDC 2393661 for ***Rac*-Qx-DPA-tBu** [Supplementary Data 5], CCDC 2393431 for ***Rac*-Pz-CZ** [Supplementary Data 6]. These data can be obtained free of charge from The Cambridge Crystallographic Data Centre via www.ccdc.cam.ac.uk/data_request/cif. Supplementary Data 7 provides all numerical source data underlying the graphs. Supplementary Data 8 to 13 provide the Cartesian coordinates in the ground state for ***MM*-Qx-CZ**, ***MM*-Qx-CZ-tBu**, ***MM*-Qx-DPA-tBu**, ***MM*-Pz-CZ**, ***MM*-Pz-CZ-tBu**, and ***MM*-Pz-DPA-tBu**, respectively. Comprehensive details on the syntheses, NMR and mass spectrometry characterization, chiral HPLC analysis, crystallographic analysis (including crystallographic tables), determination of racemization barriers, characterization of photophysical properties, electrochemical properties, thermogravimetric analysis, chiroptical properties, and theoretical calculations are provided in the Supplementary Information.

Received: 31 August 2025; Accepted: 4 December 2025;
Published online: 26 December 2025

References

1. Yoo, S. H. & Lee, H.-S. Foldectures: 3D molecular architectures from self-assembly of peptide foldamers. *Acc. Chem. Res.* **50**, 832–841 (2017).
2. Wechsel, R., Žabka, M., Ward, J. W. & Clayden, J. Competing hydrogen-bond polarities in a dynamic oligourea foldamer: a molecular spring torsion balance. *J. Am. Chem. Soc.* **140**, 3528–3531 (2018).
3. Le Bailly, B. A. F. & Clayden, J. Dynamic foldamer chemistry. *Chem. Commun.* **52**, 4852–4863 (2016).
4. Shi, C., Li, H., Shi, X., Zhao, L. & Qiu, H. Chiral pillar[n]arenes: conformation inversion, material preparation and applications. *Chin. Chem. Lett.* **33**, 3613–3622 (2022).
5. Sebaoun, L., Maurizot, V., Granier, T., Kauffmann, B. & Huc, I. Aromatic oligoamide β-sheet foldamers. *J. Am. Chem. Soc.* **136**, 2168–2174 (2014).
6. Hu, H. et al. Naphthalimide-based π-conjugated chiral foldamers: cascade-integrated construction strategy, structural analysis and chiroptical properties. *Sci. China Chem*. **68**, (2025).
7. Zhang, S. et al. Four-layer folding framework: design, GAP synthesis, and aggregation-induced emission. *Front. Chem*. **11**, (2023).
8. Tang, Y. et al. Multilayer 3D chiral folding polymers and their asymmetric catalytic assembly. *Research* **2022**, 9847949 (2022).
9. Li, J., Zhou, H. Y., Han, Y. & Chen, C. F. Saucer[n]arenes: synthesis, structure, complexation, and guest-induced circularly polarized luminescence property. *Angew. Chem. Int. Ed.* **60**, 21927–21933 (2021).
10. Hartmann, D., Penty, S. E., Zwijnenburg, M. A., Pal, R. & Barendt, T. A. A bis-perylene diimide macrocycle chiroptical switch. *Angew. Chem. Int. Ed.* **64**, e202501122 (2025).
11. Girvin, Z. C. & Gellman, S. H. Foldamer catalysis. *J. Am. Chem. Soc.* **142**, 17211–17223 (2020).
12. Jiang, C. et al. Acceptor-donor-acceptor π-stacking boosts intramolecular through-space charge transfer towards efficient red TADF and high-performance OLEDs. *Research* **2022**, 9892802 (2022).
13. Li, M. Q. et al. Regulating the spatially folded arrangement of donor and acceptor units to achieve efficient orange-red thermally activated delayed fluorescence. *Angew. Chem. Int. Ed.* **64**, e202501179 (2025).
14. Annala, R., Suhonen, A., Laakkonen, H., Permi, P. & Nissinen, M. Structural tuning and conformational stability of aromatic oligoamide foldamers. *Chem. Eur. J.* **23**, 16671–16680 (2017).
15. Teichmann, B. et al. 'Invisible' molecular dynamics revealed for a conformationally chiral π-stacked perylene bisimide foldamer. *Angew. Chem. Int. Ed.* **64**, e202414069 (2025).
16. Kaufmann, C., Bialas, D., Stolte, M. & Würthner, F. Discrete π-stacks of perylene bisimide dyes within folda-dimers: insight into long- and short-range exciton coupling. *J. Am. Chem. Soc.* **140**, 9986–9995 (2018).
17. Shen, P. et al. Switchable dual circularly polarized luminescence in through-space conjugated chiral foldamers. *Angew. Chem. Int. Ed.* **63**, e202407605 (2024).
18. Hartley, C. S. Folding of ortho-phenylenes. *Acc. Chem. Res.* **49**, 646–654 (2016).
19. Xie, Y. et al. Construction of chiral through-space luminophores via symmetry breaking triggered by sequenced chlorination. *Sci. China Chem.* **66**, 2083–2090 (2023).
20. Sun, Z. H., Tang, H., Wang, L. Y. & Cao, D. R. Advances in chiral macrocycles: molecular design and applications. *Chem. Eur. J.* **31**, e202404217 (2025).
21. Wang, Z. Y. et al. Planar chiral charge-transfer cyclophanes: convenient synthesis, circularly polarized light-responsive photothermal conversion and supramolecular chiral assembly. *Angew. Chem. Int. Ed.* **64**, e202413295 (2025).
22. Nambiar, A. P. et al. Conformationally locked cyclo[2]dipyrrins linked with anthracene subunits: synthesis and chiroptical properties. *Angew. Chem. Int. Ed.* **62**, e202306566 (2023).
23. Wang, J. et al. Tuning the (chir)optical properties and squeezing out the inherent chirality in polyphenylene-locked helical carbon nanorings. *Chem. Eur. J.* **28**, e202103828 (2022).

24. Chen, J.-F. et al. Planar chiral organoboranes with thermoresponsive emission and circularly polarized luminescence: integration of pillar[5]arenes with boron chemistry. *Angew. Chem. Int. Ed.* **59**, 11267–11272 (2020).
25. Chen, J.-F., Gao, Q.-X., Liu, L., Chen, P. & Wei, T.-B. A pillar[5]arene-based planar chiral charge-transfer dye with enhanced circularly polarized luminescence and multiple responsive chiroptical changes. *Chem. Sci.* **14**, 987–993 (2023).
26. Mathew, S. M., Engle, J. T., Ziegler, C. J. & Hartley, C. S. The role of arene–arene interactions in the folding of ortho-phenylenes. *J. Am. Chem. Soc.* **135**, 6714–6722 (2013).
27. Miller, K. A. et al. Aromatic foldamers as molecular springs in network polymers. *Chem. Commun.* **58**, 5590–5593 (2022).
28. Kinney, Z. J., Kirinda, V. C. & Hartley, C. S. Macrocycles of higher ortho-phenylenes: assembly and folding. *Chem. Sci.* **10**, 9057–9068 (2019).
29. Jiao, S. et al. Towards stable helical structures with enhanced molecular conductance by strengthening through-space conjugation. *Angew. Chem. Int. Ed.* **64**, e202414801 (2025).
30. Feng, X., Wang, X., Redshaw, C. & Tang, B. Z. Aggregation behaviour of pyrene-based luminescent materials, from molecular design and optical properties to application. *Chem. Soc. Rev.* **52**, 6715–6753 (2023).
31. Bao, L. T. et al. Rigidly locked pyrene excimers in planar chiral pyrenophanes for intense and stable circularly polarized photoluminescence and electrochemiluminescence. *Angew. Chem. Int. Ed.* **64**, e202500472 (2025).
32. Ohishi, Y. & Inouye, M. Circularly polarized luminescence from pyrene excimers. *Tetrahedron Lett.* **60**, 151232 (2019).
33. Takaishi, K., Iwachido, K. & Ema, T. Solvent-induced sign inversion of circularly polarized luminescence: control of excimer chirality by hydrogen bonding. *J. Am. Chem. Soc.* **142**, 1774–1779 (2020).
34. Takaishi, K., Takehana, R. & Ema, T. Intense excimer CPL of pyrenes linked to a quaternaphthyl. *Chem. Commun.* **54**, 1449–1452 (2018).
35. Wang, J. Y. et al. Asymmetric catalytic assembly of triple-columned and multilayered chiral folding polymers showing aggregation-induced emission (AIE). *Chem. Eur. J.* **28**, e202104102 (2022).
36. Wu, G. et al. Asymmetric catalytic approach to multilayer 3D chirality. *Chem. Eur. J.* **27**, 8013–8020 (2021).
37. Wu, G. et al. Triple-columned and multiple-layered 3D polymers: design, synthesis, aggregation-induced emission (AIE), and computational study. *Research* **2021**, 3565791 (2021).
38. Liu, Y. et al. Multi-layer 3D chirality: new synthesis, AIE and computational studies. *Sci. China Chem.* **63**, 692–698 (2020).
39. Tang, Y. et al. From center-to-multilayer chirality: asymmetric synthesis of multilayer targets with electron-rich bridges. *J. Org. Chem.* **87**, 5976–5986 (2022).
40. Jin, S. et al. Orientational chirality, its asymmetric control, and computational study. *Research* **2022**, 0012 (2022).
41. Jin, S. et al. Central-to-folding chirality control: asymmetric synthesis of multilayer 3D targets with electron-deficient bridges. *Front. Chem.* **10**, 860398 (2022).
42. Zhang, S. et al. Synthesis and characterization of multilayer 3D chiral polymers with enhanced optical properties. *Molecules* **30**, 1567 (2025).
43. Zhang, S., Yuan, Q. & Li, G. New multiple-layered 3D polymers showing aggregation-induced emission and polarization. *RSC Adv.* **14**, 13342–13350 (2024).
44. Wu, G. et al. Multilayer 3D chirality and its synthetic assembly. *Research* **2019**, 6717104 (2019).
45. Wu, G. et al. Enantioselective assembly of multi-layer 3D chirality. *Natl. Sci. Rev.* **7**, 588–599 (2020).
46. Rahman, A. U. et al. Discovery of staircase chirality through the design of unnatural amino acid derivatives. *Research* **7**, 0550 (2024).
47. Clough, R. L. & Roberts, J. D. Stable cis and trans rotational isomers of 1,8-di-o-tolylnaphthalene. *J. Am. Chem. Soc.* **98**, 1018–1020 (1976).
48. Cozzi, F., Cinquini, M., Annuziata, R. & Siegel, J. S. Dominance of polar/π over charge-transfer effects in stacked phenyl interactions. *J. Am. Chem. Soc.* **115**, 5330–5331 (1993).
49. Ringer, A. L., Sinnokrot, M. O., Lively, R. P. & Sherrill, C. D. The effect of multiple substituents on sandwich and T-shaped π–π interactions. *Chem. Eur. J.* **12**, 3821–3828 (2006).
50. Chelli, R., Gervasio, F. L., Procacci, P. & Schettino, V. Stacking and T-shape competition in aromatic–aromatic amino acid interactions. *J. Am. Chem. Soc.* **124**, 6133–6143 (2002).
51. Liu, Y., Li, C., Ren, Z., Yan, S. & Bryce, M. R. All-organic thermally activated delayed fluorescence materials for organic light-emitting diodes. *Nat. Rev. Mater.* **3**, 18020 (2018).
52. Yoo, S. & Park, Q. H. Metamaterials and chiral sensing: a review of fundamentals and applications. *Nanophotonics* **8**, 249–261 (2019).
53. Shang, X. B., Wan, L., Wang, L., Gao, F. & Li, H. Y. Emerging materials for circularly polarized light detection. *J. Mater. Chem. C.* **10**, 2400–2410 (2022).
54. Lei, Y. et al. Wide-range color-tunable organic phosphorescence materials for printable and writable security inks. *Angew. Chem. Int. Ed.* **59**, 16054–16060 (2020).
55. Li, C. et al. Deep-red to near-infrared thermally activated delayed fluorescence in organic solid films and electroluminescent devices. *Angew. Chem. Int. Ed.* **56**, 11525–11529 (2017).
56. Achelle, S., Baudequin, C. & Plé, N. Luminescent materials incorporating pyrazine or quinoxaline moieties. *Dyes Pigm* **98**, 575–600 (2013).
57. Fan, X. C. et al. Ultrapure green organic light-emitting diodes based on highly distorted fused π-conjugated molecular design. *Nat. Photon.* **17**, 280–285 (2023).
58. Lu, T. & Chen, Q. Interaction region indicator: a simple real space function clearly revealing both chemical bonds and weak interactions. *Chem. Methods* **1**, 231–239 (2021).
59. Cahn, R. S., Ingold, C. & Prelog, V. Specification of molecular chirality. *Angew. Chem. Int. Ed.* **5**, 385–415 (1966).
60. Prelog, V. & Helmchen, G. Basic principles of the CIP-system and proposals for a revision. *Angew. Chem. Int. Ed.* **21**, 567–583 (1982).
61. Takaishi, K., Iwachido, K., Takehana, R., Uchiyama, M. & Ema, T. Evolving fluorophores into circularly polarized luminophores with a chiral naphthalene tetramer: proposal of excimer chirality rule for circularly polarized luminescence. *J. Am. Chem. Soc.* **141**, 6185–6190 (2019).
62. Zhang, J. & Kürti, L. Multi-layer 3D chirality: its enantioselective synthesis and aggregation-induced emission. *Natl. Sci. Rev.* **8**, (2020).
63. Hassan, Z. et al. Planar chiral [2.2]paracyclophanes: from synthetic curiosity to applications in asymmetric synthesis and materials. *Chem. Soc. Rev.* **47**, 6947–6963 (2018).
64. López, R. & Palomo, C. Planar chirality: a mine for catalysis and structure discovery. *Angew. Chem. Int. Ed.* **61**, e202113504 (2022).
65. Patel, D. C., Woods, R. M., Breitbach, Z. S., Berthod, A. & Armstrong, D. W. Thermal racemization of biaryl atropisomers. *Tetrahedron Asymmetry* **28**, 1557–1561 (2017).
66. Lefebvre, C. et al. Accurately extracting the signature of intermolecular interactions present in the NCI plot of the reduced density gradient versus electron density. *Phys. Chem. Chem. Phys.* **19**, 17928–17936 (2017).
67. Lu, T. & Chen, Q. Independent gradient model based on Hirshfeld partition: a new method for visual study of interactions in chemical systems. *J. Comput. Chem.* **43**, 539–555 (2022).
68. Lu, T. & Chen, F. Multiwfn: a multifunctional wavefunction analyzer. *J. Comput. Chem.* **33**, 580–592 (2012).
69. Lu, T. & Chen, Q. Simple, efficient, and universal energy decomposition analysis method based on dispersion-corrected density functional theory. *J. Phys. Chem. A* **127**, 7023–7035 (2023).

70. Wu, C. et al. Face-to-face orientation of quasiplanar donor and acceptor enables highly efficient intramolecular exciplex fluorescence. *Angew. Chem. Int. Ed.* **60**, 3994–3998 (2021).
71. Li, Q. et al. Through-space charge-transfer polynorbornenes with fixed and controllable spatial alignment of donor and acceptor for high-efficiency blue thermally activated delayed fluorescence. *Angew. Chem. Int. Ed.* **59**, 20174–20182 (2020).
72. Yang, S. Y., Qu, Y. K., Liao, L. S., Jiang, Z. Q. & Lee, S. T. Research progress of intramolecular π-stacked small molecules for device applications. *Adv. Mater.* **34**, 2104125 (2022).
73. Xiang, X., Zhan, Y., Yang, W. & Jin, F. Aggregation-induced emission enhancement and mechanofluorochromism based on dicyanovinyl derivatives decorated carbazole or triphenylamine units: effects of electronic structures and spatial conformations. *Dyes Pigm* **206**, 110670 (2022).
74. Jiménez, J. et al. Modulating ICT emission: a new strategy to manipulate the CPL sign in chiral emitters. *Chem. Commun.* **55**, 1631–1634 (2019).
75. Lin, W. B., He, D. Q., Lu, H. Y., Hu, Z. Q. & Chen, C. F. Sign inversions of circularly polarized luminescence for helical compounds by chemically fine-tuning operations. *Chem. Commun.* **56**, 1863–1866 (2020).
76. Frisch, M. J. et al. Gaussian 16, Revision C.02. (Gaussian, Inc., Wallingford, CT, 2019).
77. Humphrey, W., Dalke, A. & Schulten, K. V. M. D. visual molecular dynamics. *J. Mol. Graph.* **14**, 33–38 (1996).
78. Kubo, H. et al. Tuning transition electric and magnetic dipole moments: [7]helicenes showing intense circularly polarized luminescence. *J. Phys. Chem. Lett.* **12**, 686–695 (2021).
79. Li, J.-K. et al. B,N-embedded double hetero[7]helicenes with strong chiroptical responses in the visible light region. *J. Am. Chem. Soc.* **143**, 17958–17963 (2021).

Acknowledgements

This work was financially supported by the National Natural Science Foundation of China (22161017, 22161016, 22401064, 22403022), Innovational Fund for Scientific and Technological Personnel of Hainan Province (KJRC2023D34), Hainan Provincial Natural Science Foundation of China (224QN184, 525QN257).

Author contributions

All authors have given approval to the final version of the manuscript. †These authors contributed equally, H.H. conducted organic synthesis and performed the characterizations; Q.Z. conducted theoretical calculations. CRediT: H.H. investigation, methodology, visualization, data curation, formal analysis, writing – original draft; Q.Z. software, data curation, writing – original draft; Z.W. data curation; H.L. data curation; J.X. visualization, data curation; Z.W. data curation; W.C. software; J.L. supervision, conceptualization, writing – review & editing, funding acquisition; C.J. supervision, methodology, conceptualization, writing – review & editing, funding acquisition.

Competing interests

The authors declare no competing interests.

Additional information

Supplementary information The online version contains supplementary material available at https://doi.org/10.1038/s42004-025-01855-x.

Correspondence and requests for materials should be addressed to Jianwei Li or Chunman Jia.

Peer review information *Communications Chemistry* thanks Scott Hartley and the other anonymous reviewer(s) for their contribution to the peer review of this work. A peer review file is available.